GPPS | JOURNAL

JOURNAL OF THE GLOBAL POWER AND PROPULSION SOCIETY
journal.gpps.global

Performance calculation of the thermal management system for a fuel cell aircraft engine

Review article

Article history:
Submission date: 4 November 2024
Acceptance date: 23 October 2025
Publication date: 24 February 2026

*Correspondence:
NM: niehuis@ist.rwth-aachen.de

Peer review:
Single blind

Keywords:
aircraft engine; fuel cell system; thermal management; heat exchanger

Citation:
Martin N., Peter J. (2025). Performance calculation of the thermal management system for a fuel cell aircraft engine. Journal of the Global Power and Propulsion Society. 10: 29–49.
https://doi.org/10.33737/jgpps/213543

Niehuis Martin[1,*], Jeschke Peter[1]

[1]*Institute of Jet Propulsion and Turbomachinery RWTH Aachen University, Templergraben 55, Aachen 52062, Germany*

Abstract

This paper presents a novel approach to the design of fuel cell thermal management systems, offering significant advantages for the evaluation of system architectures and design variables. The new performance calculation method considers the flow of cooling air as a separate cycle process. Analytical correlations are employed to describe the cycle process that the cooling air undergoes as it flows through the thermal management system, similar to the cycle process of an aircraft gas turbine. The power, efficiency, and other variables of the propulsion system are determined by merging the cycle processes of the propeller and the thermal management, as well as the energy conversion in the electric powertrain. We illustrate the capabilities of this approach through a sensitivity study of a small aircraft propulsion system with a required thrust of 1,000 N at a cruise speed of 85 m/s. This study examines the impact of three exemplary design variables — cooling fan pressure ratio, heat exchanger frontal area and fuel cell current density — on the overall performance of the reference propulsion system. Optimal values for these design variables have been determined to achieve maximum efficiency and minimum propulsion system mass. For example, a thermal management design without a cooling fan has a lower overall efficiency (–18.2 %) and higher mass (+17.3%) compared to a design with a cooling fan pressure ratio of 1.04. In summary, this paper presents a method for designing the thermal management of a fuel cell propulsion system and discusses the impact of design variables on engine performance. The insights provided can help engineers to optimize fuel cell propulsion system design in terms of efficiency, mass, and hydrogen consumption.

Introduction

Fuel cells powered by liquid hydrogen are a promising propulsion technology to reduce environmentally harmful emissions such as CO_2 and NO_x because the only emission from a fuel cell is its product water. Low-temperature proton-exchange membrane fuel cells (LT-PEMFCs) are considered suitable for aviation application, as they provide good efficiency (40 % to 60 %) and a reliable operation due to a high technology readiness level compared to other fuel cell types (Kazula et al., 2023). Manufacturers claim a high specific stack power of 1.5 kW/kg (ZeroAvia Inc, 2023).

Besides control, transient behavior and degradation the thermal management is one of the key challenges which have to be overcome by engineers to establish fuel cells as a competitive propulsion technology in aviation. In contrast to gas turbines or piston engines, fuel cells release only 10% to 20% of their waste heat by their exhaust flow

(Berger, 2009). With the exception of a small system power up to approximately 3 kW, fuel cell stacks must be cooled directly with a cooling fluid (Barbir, 2013). As the efficiency of the fuel cell system is about 50%, approximately the same amount of power the fuel cell provides as electric power has to be released by the thermal management. From a heat exchange perspective, the low operating temperature range of 60 °C to 90 °C of a LT-PEMFC poses an additional challenge. For hot day conditions (ISA + 25) the available temperature difference between the hot cooling fluid and the ambient air is only about 20 K to 40 K.

The large amount of waste heat and the small temperature difference result in large heat exchanger surfaces. The additional drag and weight of the heat exchanger is particularly disadvantageous for an aviation application. The challenge of cooling a fuel cell is also apparent in flying testbeds, which are equipped with large cooling air ducts that contain the heat exchangers. To either reduce the necessary heat exchanger surface by increasing the cooling air velocity or to compensate the loss of momentum of the cooling air flow, an additional cooling fan can be installed. However, it is important to note that such a cooling fan requires a significant amount of electric power, which must also be provided by the fuel cell.

Early publications on the design of fuel cell systems for aircraft propulsion have often simplified the thermal management to a function of the fuel cell power in terms of mass and power demand (Moffitt et al., 2006; Thirkell et al., 2017; Kadyk et al., 2018, 2019; Nicolay et al., 2021; Palladino et al., 2021). The additional drag due to the heat exchanger frontal area was completely neglected. Recent publications have focused on the detailed design of the thermal management system and evaluated its impact on the overall propulsion system. Kožulović (2020) has designed a heat exchanger for a mid-size airliner based on a counterflow liquid-air heat exchanger with corrugated fins. The heat exchanger is installed within a cowling with a diffusor and nozzle but without an additional fan. His analysis states that the propulsion power requirement increases by 27.3% during cruise phase due to the heat exchanger. The design is most efficient when reducing the air velocity prior to the heat exchanger to 15% of the freestream velocity. A subsequent study by Juschus (2021) is based on this approach. Hintermayr and Kazula (2023) optimized the air duct inlet of a 300 kW fuel cell system in terms of performance and sizing. They also considered an additional cooling fan to compensate the total pressure loss of the inlet section. In their studies, the fan had a power of about 20% to 95% of the fuel cell power, showing a strong dependency on the total pressure ratios of the inlet section and the heat exchanger. Hartmann et al. (2022) designed a thermal management for a fuel cell system that uses the liquid hydrogen as a heat sink. The remaining waste heat has to be dissipated by a heat exchanger with a fan. The used design approach does not rely on physics-based calculations to size the thermal management. Instead, scaling factors for the mass and the power demand by evaluating existing studies on aircraft heat exchangers have been used. Kellermann et al. (2021) designed a thermal management system using ram air and an additional cooling fan. The authors demonstrated that a fan can reduce the fuel burn for a turboelectric propulsion system and thereby increase its overall efficiency. Especially under hot conditions, the fan is beneficial in terms of reducing mass, drag, and fuel consumption. An architecture without a fan would need to be significantly larger to meet the same requirements. Eissele et al. (2023) used the results of Kellermann et al. (2021) to develop a scaling factor for the heat exchanger drag. They applied this scaling factor to a fuel cell propulsion system as part of an overall aircraft design but neglected the additional power demand.

Overall, the thermal management causes additional drag, weight and electric power demand in a relevant order of magnitude. The performance of the propulsion system is directly affected by the design of the heat exchanger and the cooling fan. Therefore, the thermal management design cannot be covered by simple scaling factors in the performance calculation of a fuel cell propulsion system but must be integrated into the design process.

This paper is structured as follows: The methodology for calculating the performance is presented first. This includes the definition of the cycle processes, the development of the applied component models and the design algorithm to solve the design problem. In the next section we conduct a design exploration study for typical design variables to demonstrate the benefits of the novel performance calculation approach. Finally, the results of the study for a reference propulsion system are presented and discussed.

Methodology

First, we give a brief introduction to the propulsion system under study. Then, we examine the cycle process of the propeller and the thermal management. By combining the energy conversion and the cycle processes, we derive general equations for the performance calculation of a fuel cell propulsion system. Similar to conventional propulsion systems we define thrust, efficiency and specific fuel consumption. To calculate the thermodynamic processes between the separate stations as well as the energy conversion of the fuel cell powertrain we develop

component models. The methodology section concludes with a description of the iterative design calculation process that uses the component models to solve the cycle processes.

Performance calculation

This section describes the performance calculation of the fuel cell propulsion system. We first examine the energy conversion in the powertrain system from the hydrogen tank to the shaft power of the propeller and the resulting conversion losses. Next, we analyze the propeller and the thermal management by interpreting them as two independent cycle processes. The stations for each process are defined, and the state changes are sketched in the *h*,*s*-diagram. The derivation of thrust, power and efficiency is based on this diagram, following the conventional aircraft performance calculation method explained by Jeschke et al. (2024). The cycle processes and energy conversion by the powertrain are then merged to the overall propulsion system.

Fuel cell powertrain

The fuel cell powertrain is shown in Figure 1. A cryogenic tank supplies hydrogen with the power P_{H_2} to the LT-PEMFC. The thermal insulation and vaporization of liquid hydrogen is not the subject of this publication. The fuel cell converts the electrochemically stored energy of the hydrogen into the electric power P_{FCS} and provides it as direct current (DC). To decouple the fuel cell and the further electric components in terms of their operation voltage, a DC/DC converter transforms the fuel cell output power to the DC link voltage. The inverter transforms the DC link voltage into a three-phase alternating current (AC) for the electric motor. The electric motor converts the AC voltage power P_{IV} into the mechanical shaft power P_{EM}. A gearbox between the electric motor and the propeller enables an additional degree of freedom regarding the rotational speed of the electric motor. This allows the use of a high-speed and therefore power-dense electric motor. Finally, the propeller is driven by the mechanical shaft power P_P.

In addition to the powertrain path, the DC bus also supplies power to additional loads. This includes the power required by the cooling air fan, denoted as P_C in this study. A battery is typically connected via a DC/DC converter and serves as a buffer to meet dynamic power requirements. However, since this study only examines stationary operating points, the battery is not considered in the following investigations. Following Figure 1, we establish the power balance around the DC bus by applying the efficiencies of the electrical components. The consumers are placed on the left-hand side of the equation, and the source is placed on the right-hand side to relate the power to the DC bus

$$\frac{P_P}{\eta_{IV}\eta_{EM}\eta_{GB}} + \frac{P_C}{\eta_{DC}\eta_{EM,C}} = P_{H_2}\eta_{FCS}\eta_{DC}. \tag{1}$$

During the numerous energy conversions, losses depending on the component efficiencies η occur. These losses are summarized in the power loss of the energy conversion system $\dot{Q}_{loss}$, which is transferred to the thermal management

$$\dot{Q}_{loss} = \dot{Q}_{in,TM}. \tag{2}$$

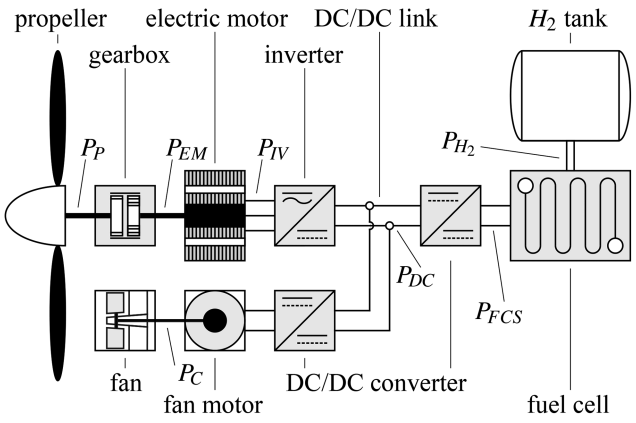

Figure 1. Architecture of a fuel cell propulsion system for aerospace application.

Cycle process of the propeller

Figure 2 shows the stations of the propeller cycle process (Figure 2a) and the thermodynamic state changes in the *h*,*s*-diagram (Figure 2b). In station 0, the propeller draws in air from the surrounding environment. The inlet flow tube contracts in front of the propeller, transitioning isentropically to station 12. Between stations 12 and 13, the propeller performs the specific propeller work a_P, resulting in the propeller power

$$P_P = \dot{m}_P a_P = \dot{m}_P (h_{t13} - h_{t12}) \tag{3}$$

with the propeller mass flow $\dot{m}_P$. The resulting increase in total pressure is expressed by the propeller total pressure ratio

$$\pi_P = \pi_{12,13} = \frac{p_{t13}}{p_{t12}}. \tag{4}$$

However, the supplied power is not isentropically converted into a total pressure increase. Therefore, we define the isentropic propeller efficiency

$$\eta_{P,s} = \frac{h_{t13s} - h_{t12}}{h_{t13} - h_{t12}} = \frac{h_{t13s} - h_{t12}}{a_P}. \tag{5}$$

Similarly, the isentropic nozzle efficiency $\eta_{N,s}$ is defined for the change of state from 13 to 19. The usable output power of the cycle process is defined as

$$P_{out,P} = \dot{m}_P \left(\frac{c_0^2 - c_{19}^2}{2} \right), \tag{6}$$

which leads us to the thermal efficiency of the propeller with Equation 3

$$\eta_{th,P} = \frac{-P_{out,P}}{P_P} = -\frac{c_0^2 - c_{19}^2}{2(h_{t13} - h_{t12})}. \tag{7}$$

As the static pressures upstream and downstream of the propeller are equal ($p_0 = p_9$), the propeller thrust is calculated by

$$F_P = \dot{m}_P (c_{19} - c_0), \tag{8}$$

which leads us to the propulsion power

$$P_{F,P} = F_P c_0. \tag{9}$$

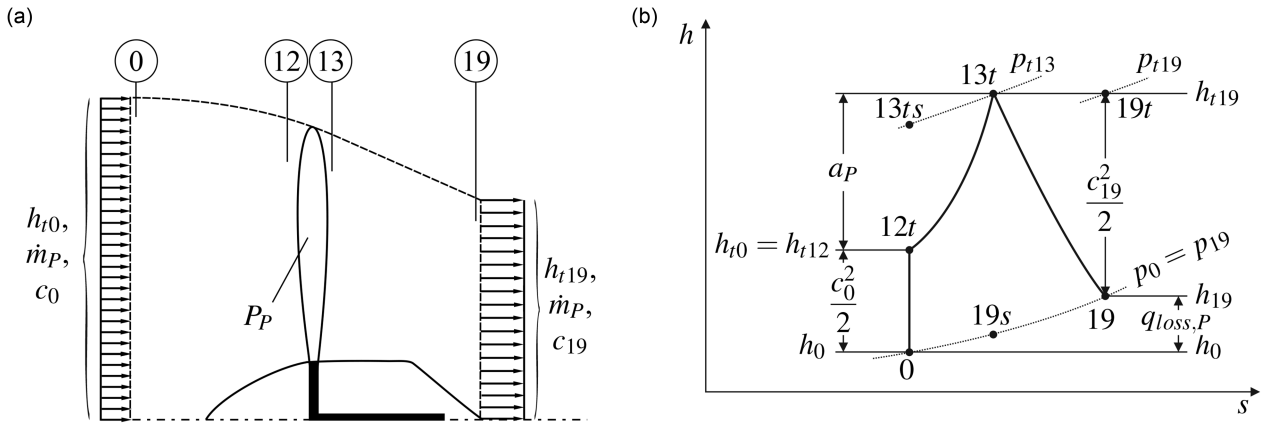

Figure 2. Cycle process of the propeller of an aircraft fuel cell propulsion system. (a) Stations and (b) Thermodynamic changes in *h*, *s*-diagram.

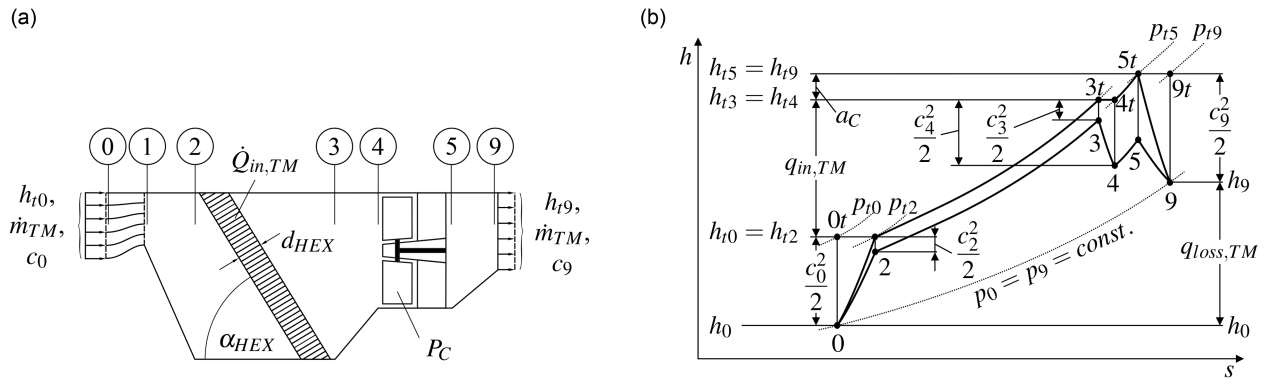

Figure 3. Cycle process of the thermal management of an aircraft fuel cell propulsion system. (a) Stations and (b) Thermodynamic changes in h, s-diagram.

With the equations above the cycle process of the propeller is completely defined.

Cycle process of the thermal management

Figure 3 presents the stations of the thermal management cycle process (Figure 3a) and the thermodynamic state changes in the h,s-diagram (Figure 3b). The illustration shows the schematic cowling of the heat exchanger and fan. The cowling is designed for low aerodynamic drag, as described by Drela (1996). From station 0 to 2 the ambient air is decelerated in a diffusor to increase the static pressure in front of the heat exchanger. The total pressure losses due to the expansion are considered by

$$\pi_{0,2} = \frac{p_{t2}}{p_{t0}}. \tag{10}$$

In the heat exchanger from station 2 to 3 the power loss of the energy conversion system Equation 2 is transferred to the cooling air mass flow $\dot{m}_{TM}$, leading to an increase in enthalpy

$$h_{t3} - h_{t2} = q_{in,TM} = \frac{\dot{Q}_{in,TM}}{\dot{m}_{TM}}. \tag{11}$$

Due to inner wall friction as well as expansion and compression of the cooling air, a total pressure loss occurs across the heat exchanger

$$\Delta p_{t2,3} = p_{t3} - p_{t2} \tag{12}$$

that is a function of the geometry, fin design, air flow and fluid properties. To decouple the cross sections of the heat exchanger and the cooling fan, a transition duct from station 3 to 4 with the total pressure ratio

$$\pi_{t3,4} = \frac{p_{t4}}{p_{t3}}. \tag{13}$$

is assumed. Between station 4 and 5 a cooling fan with the total pressure ratio

$$\pi_C = \pi_{t4,5} = \frac{p_{t5}}{p_{t4}} \tag{14}$$

and the isentropic efficiency $\eta_{C,s}$, see Equation 5, performs the specific cooling fan work a_C, resulting in the cooling fan power

$$P_C = \dot{m}_{TM} a_C = \dot{m}_{TM}(h_{t5} - h_{t4}). \tag{15}$$

Figure 3b demonstrates that the air is perfectly compressed or expanded to ambient pressure ($p_0 = p_9$) in an ideal nozzle from station 5 to 9, resulting in a loss of total pressure

$$\pi_{t5,9} = \frac{p_{t9}}{p_{t5}}. \tag{16}$$

For this cycle process, we define the power input and output. The usable output power of the cycle process is defined as

$$P_{out,TM} = \dot{m}_{TM}\left(\frac{c_0^2 - c_9^2}{2}\right). \tag{17}$$

As there is a difference in velocity of the air between the inlet and outlet, the cooling air mass flow generates a force

$$F_{TM,int} = \dot{m}_{TM}(c_9 - c_0). \tag{18}$$

The cowling which covers heat exchanger and cooling fan creates an additional drag $F_{TM,ext}$. As this force may account for a significant portion of the propeller's thrust Equation 8 it must be included in the performance calculation. For the calculation of this force, refer to the section on component models and Equation 44. With the thrust of the thermal management

$$F_{TM} = F_{TM,int} + F_{TM,ext} \tag{19}$$

we calculate its propulsion power

$$P_{F,TM} = F_{TM} c_0. \tag{20}$$

Overall propulsion system

The energy conversion processes of the powertrain and propeller, along with the thermal management cycle, have been fully defined. The next step is to aggregate the equations of the three subsystems to calculate the power, thrust, and efficiency of the entire fuel cell propulsion system. The overall usable output power is calculated with Equations 6 and 17

$$\begin{aligned} P_{out} &= P_{out,P} + P_{out,TM} \\ &= \dot{m}_P\left(\frac{c_0^2 - c_{19}^2}{2}\right) + \dot{m}_{TM}\left(\frac{c_0^2 - c_9^2}{2}\right). \end{aligned} \tag{21}$$

With Equation 21 and the supplied hydrogen power P_{H_2}, that we will derive later Equation 34, we get the thermal efficiency of the overall powertrain

$$\eta_{th} = \frac{-P_{out}}{P_{H_2}}. \tag{22}$$

The total thrust of the fuel cell propulsion system consists of Equations 8 and 19

$$F = F_P + F_{TM}. \tag{23}$$

We also define the specific fuel consumption

$$SFC = \frac{\dot{m}_{H_2}}{F} \tag{24}$$

with the hydrogen mass flow $\dot{m}_{H_2}$, which we introduce later Equation 33. The overall propulsion power is defined as sum of Equations 9 and 20

$$P_F = P_{F,P} + P_{F,TM} = Fc_0, \tag{25}$$

with which we calculate the propulsion efficiency

$$\eta_p = \frac{P_F}{-P_{out}} = \frac{2}{1 + \frac{c_{19}}{c_0}} + \frac{2}{1 + \frac{c_9}{c_0}} \tag{26}$$

and finally the overall efficiency of propulsion system

$$\eta_o = \eta_{th}\eta_p = \frac{P_F}{P_{H_2}}. \tag{27}$$

Component models

Next, we develop component models which describe the energy conversion and thermodynamic changes of state.

Fuel cell system

As shown in the Figure 1, the fuel cell provides the net electrical power P_{FCS}. A comprehensive model of the auxiliary electric consumers of the fuel cell like the air compressor, as described by Schmelcher and Häßy (2022), is omitted. Instead, the power demand is expressed via the factor f_{aux}. The gross power to be generated is then calculated as

$$P_{FCS,gr} = \frac{P_{FCS}}{1 - f_{aux}}. \tag{28}$$

The fuel cell system consists of multiple stacks, which in turn consist of multiple cells. The operating point of a cell is defined by its current density

$$i_{cell} = \frac{I_{cell}}{A_{act,cell}}, \tag{29}$$

which relates the current I_{cell} to the active area $A_{act,cell}$ of a cell. The cell voltage U_{cell} is calculated by subtracting all losses from the theoretical voltage under standard conditions U_{th}^0. It is assumed that the stack is operated at a constant pressure of $p_{stack} = 3\text{bar}$. The calculation of U_{cell} has been implemented according to Barbir (2013). The resulting polarization curve then provides U_{cell} as a function of i_{cell} and with

$$P_{cell} = U_{cell}I_{cell} = U_{cell}i_{cell}A_{act,cell} \tag{30}$$

we also get the electric power generated by a single cell. With Equation 28 we calculate the number of cells needed

$$n_{cell} = \frac{P_{FCS,gr}}{P_{cell}} = \frac{\frac{P_{FCS}}{1 - f_{aux}}}{U_{cell}i_{cell}A_{act,cell}}. \tag{31}$$

Having defined the operating point and the design of the fuel cell we now calculate the hydrogen consumption of the fuel cell system. The reaction equation of the fuel cell provides the charge number of hydrogen as $z_{H_2} = 2$, see Appendix A. With the Faraday's law, the Faraday constant F and the molar mass M_{H_2} of hydrogen we get the stoichiometric hydrogen mass flow per cell

$$\dot{m}_{H_2,cell} = \frac{I_{cell}}{z_{H_2}F}M_{H_2} \tag{32}$$

and for the fuel cell system with the number of cells from Equation 31

$$\dot{m}_{H_2} = n_{cell}\dot{m}_{H_2,cell}. \tag{33}$$

The formula to calculate the hydrogen mass flow is derived in Appendix B. In real operation, more hydrogen is supplied than required for the stoichiometric ratio. In this study, we assume the use of a fuel cell with hydrogen recirculation. Any excess hydrogen that is not consumed is not considered in the fuel calculation as it remains within the system. With Equation 33 and the lower heating value of hydrogen LHV_{H_2} we are able to calculate the supplied hydrogen power

$$P_{H_2} = \dot{m}_{H_2} LHV_{H_2} \tag{34}$$

and the efficiency of the fuel cell system as

$$\eta_{FCS} = \frac{P_{FCS}}{P_{H_2}} = \frac{P_{FCS}}{\dot{m}_{H_2} LHV_{H_2}}. \tag{35}$$

The fuel cell system's total power loss is determined by

$$\dot{Q}_{loss,FCS} = P_{H_2} - P_{FCS}. \tag{36}$$

A part of the supplied fuel power is released into the environment as waste heat via the exhaust gas flow expressed by the factor $f_{loss,ext} = 5\%$ to 10% (Berger, 2009). This reduces the amount of waste heat that actually needs to be cooled by the thermal management to

$$\dot{Q}_{TM,FCS} = \dot{Q}_{loss,FCS} - P_{H_2} f_{loss,ext}. \tag{37}$$

The mass of the fuel cell system

$$m_{FCS} = p_{FCS} P_{FCS} \tag{38}$$

is calculated with the specific power p_{FCS} which is a function of i_{cell}.

Heat exchanger

The heat exchanger is illustrated in Figure 3a from station 2 to 3. We assume a plate-fin heat exchanger with offset fins. This is a crossflow heat exchanger with thin fins attached to its plates to increase the heat exchange surface to the passing air. The fins do not run in a longitudinal direction through the entire depth of the heat exchanger. Instead, they end after a certain distance and are offset to the side. This design interrupts the boundary layer formation of the passing cooling air and thus increases the heat transfer. Depending on the heat exchanger's design, the offsets may be repeated multiple times. This heat exchanger type is appropriate for transferring heat from liquid to gas. It is distinguished by a large heat transfer surface area per unit volume and high heat transfer coefficients at Reynolds numbers ranging from $Re = 500$ to 10,000. Plate-fin heat exchangers with offset fins are commonly used in mobile applications, such as passenger vehicles and airplanes, due to their high specific power resulting from the thin-walled channel and fin structure (Shah and Sekulić, 2003). The heat flux transferred by the heat exchanger is calculated using the $\varepsilon - NTU$ method described by Kays and London (2018) and Kakaç et al. (2012). The actually transferred heat power

$$\dot{Q}_{TM,in} = \varepsilon \dot{Q}_{max} \tag{39}$$

is defined as the product of the heat exchanger effectiveness ε and the theoretical maximum transferable heat power $\dot{Q}_{\max}$ that depends on the fluid mass flows, their heat capacities and temperatures. ε is calculated using a correlation that depends on the flow arrangement and the number of transfer units NTU

$$NTU = \frac{UA}{C_{min}}. \tag{40}$$

$C_{\min}$ is the minimum capacity heat rate. The product of the overall heat transfer coefficient U and the exchange surface A is broken down into three partial heat transfers

$$\frac{1}{UA} = \underbrace{\frac{1}{\eta_a h_a A_a}}_{\text{air side}} + \underbrace{\frac{\delta_w}{\lambda_w A_w}}_{\text{wall}} + \underbrace{\frac{1}{h_f A_f}}_{\text{coolant side}} . \tag{41}$$

A is the surface area and h is the heat transfer coefficient of the respective side. η_a is the surface efficiency of the air side with offset fins. Heat conduction in the walls is also taken into account. To calculate η_a, A, and h, respectively, we use correlations for plate-fin heat exchangers with offset fins and rectangular channels published by Manglik and Bergles (1995) and Shah and Sekulić (2003).

The pressure loss across the heat exchanger defined in Equation 12 is comprised as

$$\Delta p_{2,3} = \Delta p_{HEX} = \Delta p_{in} + \Delta p_{core} - \Delta p_{out}, \tag{42}$$

consisting of three parts for the inflow into the heat exchanger, the friction in the core and the outflow according to Shah and Sekulić (2003). The core loss accounts for the largest share

$$\Delta p_{core} = \frac{G^2}{2\rho_2}\left(2\left(\frac{\rho_2}{\rho_3} - 1\right) + f\frac{d_{HEX}}{r_{hyd}}\frac{\rho_2}{\rho_{\overline{23}}}\right) \tag{43}$$

significantly influenced by the Fanning friction factor f. The friction factor for offset fin heat exchangers is a function of Re and the fin geometry as stated by Manglik and Bergles (1995). The design calculation maintains constant geometric ratios of the fins, which have been calibrated using a real aviation heat exchanger (Rotax, 2021). The heat exchanger is scaled only via its cross-sectional area A_{HEX}, with a constant height-to-side ratio, and its depth d_{HEX}. The geometric constants of the fin, A_{HEX} and d_{HEX}, are also used to determine the wet mass of the heat exchanger m_{HEX}, assuming aluminum as the material. The mass flow of the coolant is proportionally adjusted based on $\dot{m}_{TM}$ using a constant ratio. The coolant side of the thermal management is not taken into account in the power balance, as the power demand is negligible compared to the air side (Kellermann et al., 2021).

Cowling

The external drag of the cowling is calculated using a drag coefficient $c_{D,TM}$ based on the shape and installation of the cowling, the effective frontal area of the heat exchanger $A_{HEX,fr}$, and ambient air data (ρ_0,c_0)

$$F_{TM,ext} = -\frac{1}{2} c_{D,TM} A_{HEX,fr} \rho_0 c_0^2. \tag{44}$$

Thrust is considered positive when the force acts in the direction of flight. Therefore, it is necessary to include a negative sign. Hoerner (1965) gives typical values for drag coefficients of belly-type radiator installations and therefore we define $c_{D,TM} = 0.06$. The wall thickness of the cowling is neglected and the frontal area of the heat exchanger is assumed to be the frontal area of the cowling. To reduce the frontal area and, because of Equation 44, also $F_{TM,ext}$, the heat exchanger is installed under an inclination angle α_{HEX} as shown in Figure 3a. This installation reduces the effective frontal area to

$$A_{HEX,fr} = \sin(\alpha_{HEX}) A_{HEX} \tag{45}$$

Since the air always flows perpendicular to A_{HEX}, the cooling air mass flow must be deflected by the angle α_{HEX} before and after the heat exchanger. The discharge coefficient to calculate the total pressure loss of the inlet and outlet deflection is estimated according to Bohl and Elmendorf (2013).

Further propulsion system components

This study does not focus on the powertrain components, such as the electric motor, inverter, and DC/DC converter. Therefore, constant efficiencies and power densities are assumed in the design process. The data utilized in this study are presented in Appendix F. The mass of the gearbox is calculated using a correlation from Brown

et al. (2005). A correlation by Chapman et al. (2020) is used for the mass of the cooling fan. The propeller mass was calculated using a correlation from LTH (2022).

Design calculation process

The flowchart of the design process is shown in Appendix C. It is important to note that some of the variables to be calculated are interdependent. For instance, the power of the cooling air fan P_C is influenced by $\dot{m}_{TM}$, see Equation 15, which affects P_{FCS} and thus $\dot{Q}_{TM,FCS}$. $\dot{Q}_{TM,FCS}$ in turn has an influence on the required $\dot{m}_{TM}$. Therefore, the problem must be solved iteratively. At the start of the process, the requirements, design variables, boundary conditions, and estimated initial values are established as input data. This data is employed for the initial design calculations of the propeller from stations 0 to 19 and the thermal management system from stations 0 to 9. Subsequently, the remaining powertrain components and the fuel cell system are designed. Next, the actual power loss $\dot{Q}_{loss}$, which was initially estimated, and the total thrust of the propulsion system F are calculated. The cooling air mass flow $\dot{m}_{TM}$ is iterated until the power loss of the propulsion system $\dot{Q}_{loss}$ is equal to the heat output transferred by the heat exchanger $\dot{Q}_{TM,in}$ according to Equation 2. To fairly compare designs and sensitivities, the resulting total thrust F must be constant for all parameter combinations. Because the design of the thermal management affects F, see Equation 23, the design calculation is embedded in another loop that iteratively sizes the propeller until the required thrust F is achieved.

Results and discussion

The design methodology described in this paper is applied to a reference propulsion system. The sensitivities in relation to the thermal management and the overall propulsion system are then discussed by varying three exemplary design variables.

Reference propulsion system

A small four-seater aircraft is used as reference application. Table 1 summarizes the design requirements and environmental conditions for the selected design point during cruise flight. The requirements are derived from typical general aviation aircraft and are otherwise arbitrarily defined. We assume here, that the fuel cell system is designed for the cruise operation point, while a battery provides additional power for take-off and climb. An exemplary design that fulfills the requirements of Table 1 is presented in Table 2. The data utilized for the design of the fuel cell are listed in Appendix D. The resulting polarization curve is presented in Appendix E. The remaining parameters for the powertrain components, which were assumed to be constant for the reference design and the design exploration study, are listed in Appendix F. We now apply the design methodology described and the reference values from Table 2 to the performance requirements and boundary conditions during cruise flight from Table 1. Thereby we obtain the performance data of our reference design as shown in Table 3 that serves as a reference for the following studies.

Design space exploration

By exemplarily varying the design variables π_C, A_{HEX}, and i_{cell}, the sensitivities on the thermal management and the resulting deviations of the performance data from the reference design (Table 3) are discussed.

Table 1. Performance requirements and boundary conditions during cruise flight.

Parameter	Value
Thrust F	1,000 N
Altitude ALT	3,000 m
Ambient condition	ISA + 15 K
Airspeed c_0	85 m/s

Table 2. Design variables and their reference values.

Parameter	Value
Cooling fan total pressure ratio π_C	1.04
Heat exchanger cross section A_{HEX}	0.90 m^2
Heat exchanger depth d_{HEX}	0.15 m
Heat exchanger inclination angle α_{HEX}	20°
Fuel cell current density i_{cell}	1.40 A/cm^2

Total pressure ratio of the cooling fan π_C

The results of varying π_C are shown in Figure 4 for the thermal management and in Figure 5 for the overall system. Since the external thermal management drag $F_{TM,ext}$ is not a function of π_C according to Equation 44, it remains constant. Due to losses in the cooling air duct and heat exchanger $F_{TM,int}$ is negative for $\pi_C < 1.04$. As π_C increases, a higher total pressure is available downstream of the fan to be converted into thrust in the nozzle. Initially, this only compensates for the internal total pressure loss. At high values of $\pi_C > 1.05$, $F_{TM,ext}$ is fully compensated. From this total pressure ratio and above, the thermal management generates positive thrust F_{TM}. It is evident that both $F_{TM,int}$ and $F_{TM,ext}$ contribute significantly to the required thrust of $F = 1{,}000$ N (Table 1). Therefore, it is justified to include the thermal management in the performance calculation.

Contrary to expectations, $\dot{m}_{TM}$ does not increase as π_C increases since the thrust nozzle is controlled to only pass the mass flow actually required for cooling. Therefore, $\dot{m}_{TM}$ depends on the efficiency of the propulsion system, which is influenced by the π_C, as we will discuss later. As $\dot{m}_{TM}$ is almost constant, P_C increases proportionally to π_C. The thermal management system's mass m_{TM} increases only slightly with an increasing π_C due to the larger fan because the unchanged heat exchanger accounts for the majority of m_{TM}.

Figure 5 illustrates that η_p is highly dependent on π_C. Initially, increasing π_C to 1.04 leads to a rapid increase in η_p due to a significant reduction in the absolute value of $F_{TM,int}$, as shown in Figure 4. This reduction causes a significant decrease in the additional thrust required by the propeller to compensate for drag, leading to a smaller dimensioned powertrain and thermal management. As η_{th} remains nearly constant, η_o follows the same trend as η_p. A fuel cell propulsion system without a cooling air fan ($\pi_C = 1.00$) would have an η_o which is 18.2% lower than the reference design. The fan's increasing power P_C leads to a snowball effect starting at

Table 3. Performance data of the reference propulsion system.

Parameter	Value
Overall efficiency η_o	22.5%
Propulsive efficiency η_p	91.3%
Thermal efficiency η_{th}	24.6%
Specific fuel consumption *SFC*	3.15 g/(kNs)
Cooling fan power P_C	22.8 kW
Total mass m	196.6 kg
Thermal management mass m_{TM}	78.5 kg

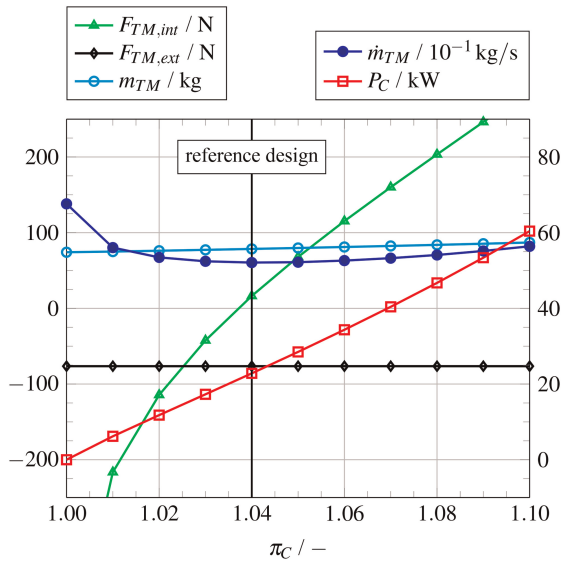

Figure 4. Plot of $\dot{m}_{TM}$, P_C, $F_{TM,ext}$, $F_{TM,ext}$ and m_{TM} over π_C; values of the variables in the left legend are displayed on the left ordinate axes and vice versa.

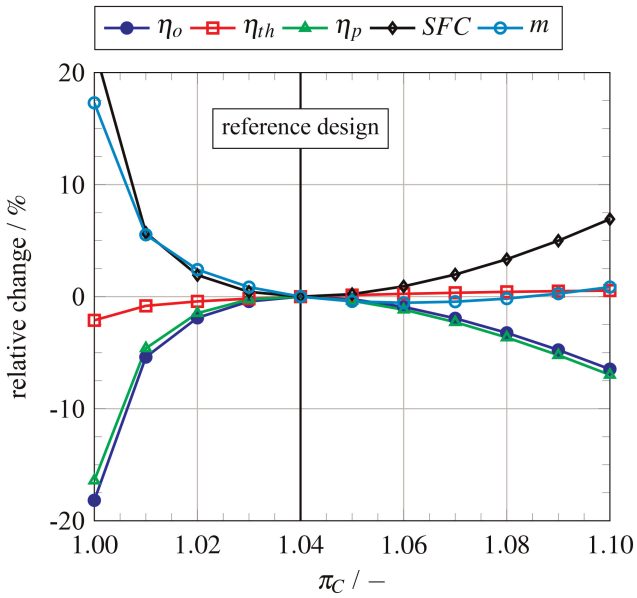

Figure 5. Plot of the relative change from the reference design (Table 3) of η_o, η_p, η_{th}, SFC and m over π_C.

m_{TM}: the fuel cell's output power and loss both increase. The increased cooling power required results in a higher $\dot{m}_{TM}$ (Figure 4), which in turn increases P_C and because of Equation 1 also P_{FCS}. Consequently, η_o decreases beyond a pressure ratio of $\pi_C = 1.04$. The specific fuel consumption SFC is inversely related to η_o. Therefore, it increases for small or large values of π_C and also has a minimum at the reference design point.

As π_C increases, the total mass m initially decreases. Figure 4 demonstrates that the fan compensates for the drag of the thermal management, resulting in smaller dimensions of the powertrain components and the fuel cell as already discussed. A fuel cell propulsion system without a fan would have a 17.3% higher total mass compared to the reference design. At $\pi_C = 1.06$, m reaches its minimum approximately 0.5% below the reference. Further increase in π_C requires more power for the fan P_C (see Figure 4), which must be provided by the fuel cell. Therefore, the mass of the fuel cell increases again from the reference design. This leads to a compensation for the mass reduction of the powertrain, resulting in a net increase of m from $\pi_C = 1.06$.

Cross section area of the heat exchanger A_{HEX}

The variation of the heat exchanger area in Figure 6 starts at $A_{HEX} = 0.6$ m^2. This is the smallest possible value at which a sufficient cooling power is achieved. A small A_{HEX} requires a higher $\dot{m}_{TM}$ and P_C to transfer the necessary cooling capacity due to high Reynolds numbers and a smaller heat transfer surface. As A_{HEX} increases, the required $\dot{m}_{TM}$ and P_C decrease. From Equation 44 it is evident that $F_{TM,ext}$ increases as A_{HEX} increases. m_{TM} is mainly determined by the heat exchanger, which results in an almost linear increase despite the decreasing fan mass.

To compensate for the increasing $F_{TM,ext}$, the propeller must provide more thrust. While the power of the propeller increases with larger heat exchanger surfaces, the power demand for the thermal management increases with smaller heat exchangers. This leads to an optimum of η_o and total mass m as shown in Figure 7. The lowest possible m at $A_{HEX} = 0.7$ m^2 is achieved with a smaller heat exchanger surface compared to the optimum η_o at $A_{HEX} = 1.1$ m^2. Compared to the reference design, a thermal management system with the smallest possible heat exchanger has a 4.5% lower mass but a 10.3% lower η_o. The optimum η_o for our study is achieved at $A_{HEX} = 1.1$ m^2. For this heat exchanger size η_o is 0.7% higher and m is 7.2% higher compared to the reference design.

Current density of the fuel cell system i_{cell}

The cell current density i_{cell} is varied to analyze its influence on the thermal management (Figure 8) and the overall system (Figure 9). The polarization curve of the designed fuel cell (Appendix E) indicates that the cell power P_{cell} initially increases with increasing i_{cell}, accompanied by an increase in losses. Therefore, a low i_{cell}

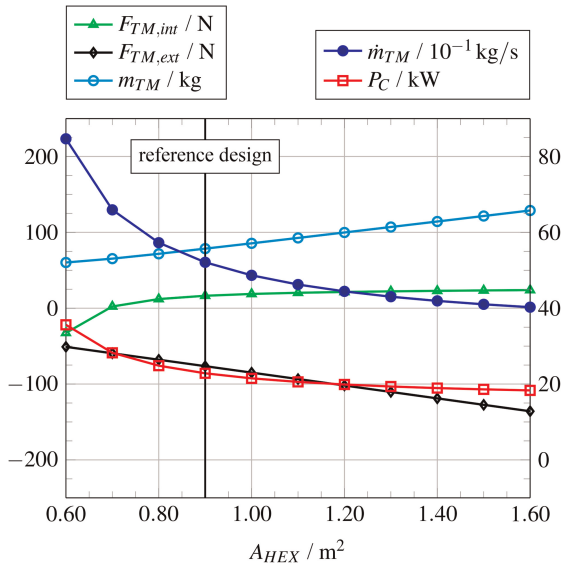

Figure 6. Plot of $\dot{m}_{TM}$, P_C, $F_{TM,ext}$, $F_{TM,ext}$ and m_{TM} over A_{HEX}; values of the variables in the left legend are displayed on the left ordinate axes and vice versa.

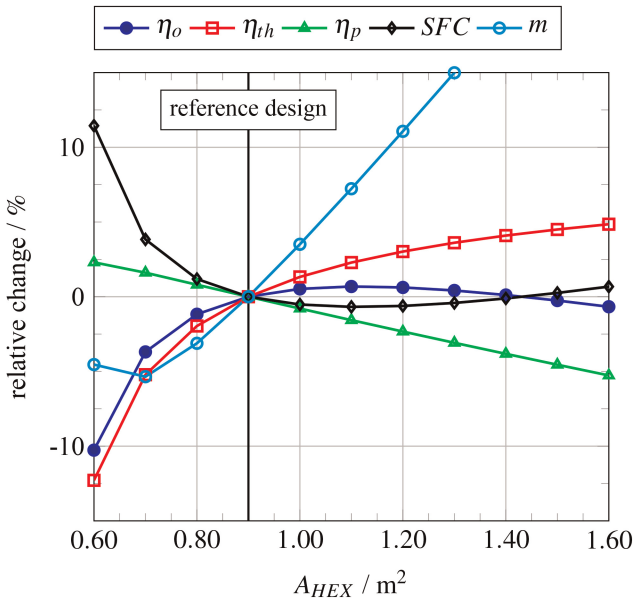

Figure 7. Plot of the relative change from the reference design (Table 3) of η_o, η_p, η_{th}, SFC and m over A_{HEX}.

corresponds to an efficient cell, while a high i_{cell} corresponds to a power-dense cell. The necessary $\dot{m}_{TM}$ must also increase to achieve a sufficiently high cooling capacity. This results in an increase in P_C and m_{TM} (Figure 8), despite the heat exchanger accounting for a large portion of the thermal management mass. At a high current density ($i_{cell} > 1.4$ A/cm^2), concentration polarization losses increase significantly, leading to a decrease in both efficiency and P_{cell}. As the current density increases, so does the thermal power transferred to the cooling air, resulting in an increase in $F_{TM,int}$, which is known as the *Meredith effect*. However, at values of $i_{cell} > 1.4$ A/cm^2, the nozzle must be opened wider to allow for the necessary $\dot{m}$, which in turn leads to a lower c_9 and a reduction in thrust as described by Equation 18. Increasing the load on the cell from 0.6 A/cm^2 to 1.4 A/cm^2 results in an increase in cooling air mass flow $\dot{m}_{TM}$ by a factor of 2. The drag resistance $F_{TM,ext}$ remains constant due to the unchanged heat exchanger geometry (Figure 8).

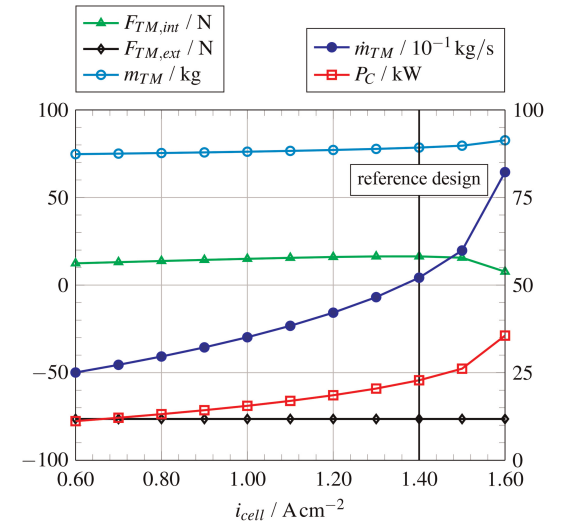

Figure 8. Plot of $\dot{m}_{TM}$, P_C, $F_{TM,ext}$, $F_{TM,ext}$ and m_{TM} over i_{cell}; values of the variables in the left legend are displayed on the left ordinate axes and vice versa.

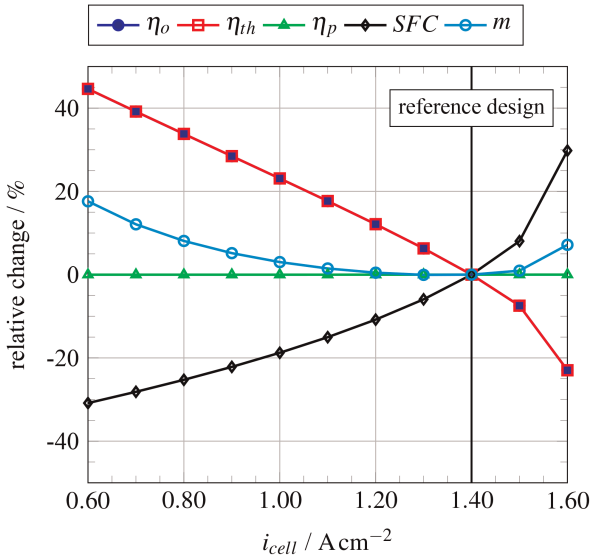

Figure 9. Plot of the relative change from the reference design (Table 3) of η_o, η_p, η_{th}, SFC and m over i_{cell}.

Figure 9 illustrates that η_{th} decreases as i_{cell} increases due to the rising losses in the fuel cell. η_p remains almost constant, resulting in η_o following the same dependency as η_{th} on i_{cell}. Additionally, m decreases initially as the cell's power density becomes higher. The sharp loss of power at high current densities, see Appendix E, must be compensated by a larger sized fuel cell system, so that m increases again compared to the reference design (Figure 9). Therefore, the cell should only be designed for $i_{cell} < 1.4\ \mathrm{A/cm^2}$, as a higher i_{cell} leads to increased m and decreased η_o. Compared to the reference, a 33.8% higher η_o can be achieved with $i_{cell} = 0.8\mathrm{A/cm^2}$ at an increase of 8.1% in m.

Conclusion

This paper illustrates the integration of the thermal management for a fuel cell propulsion system into the engine performance calculation. The thermal management air path is treated as a separate cycle, similar to conventional engines. Together with the propeller cycle process and the energy conversion from hydrogen to mechanical propeller power, key performance data of the engine performance calculation for the fuel cell powertrain are thus derived. Physically scalable models have been developed for the powertrain and the thermal management components. These models describe the changes in state of the cycle processes and the conversion of energy as a function of their design variables.

The capabilities of the presented method are demonstrated by a design space exploration. First, the fuel cell powertrain system and the thermal management are designed for a small aircraft as a reference application. The reference aircraft engine has an overall efficiency of $\eta_o = 22.5\%$ and a mass of $m = 196.6$ kg, of which 78.5 kg are accounted for by the thermal management system. Three exemplary design variables — cooling fan pressure ratio π_C, heat exchanger surface A_{HEX} and fuel cell current density i_{cell} — are varied. The sensitivities in relation to the thermal management and the overall aircraft engine are discussed. The thermal management causes high drag due to internal total pressure losses and external pressure drag of the cowling. To address this issue, the reference design includes an additional cooling air fan located behind the heat exchanger with a total pressure ratio $\pi_C = 1.04$. It was shown that the design of the thermal management has a major influence on the performance data of the propulsion system. A design lacking a fan ($\pi_C = 1.00$) has a lower overall efficiency η_o by 18.2% and higher total mass m by 17.3%. An optimal A_{HEX} in terms of efficiency has also been identified. This is caused by increasing fan power P_C for small heat exchangers and increasing propeller power P_P to overcome the drag of a large heat exchanger. By varying i_{cell}, it was shown how an efficient cell influences the thermal management design compared to a power-dense cell. Increasing the load on the cell from 0.6 $\mathrm{A/cm^2}$ to 1.4 $\mathrm{A/cm^2}$ results in a two times higher cooling air mass flow $\dot{m}_{TM}$. With regard to the overall propulsion system, it is stated that at lower current densities, a trade-off between increasing efficiency and mass compared to the reference design must be considered, e.g. a 33.8% higher η_o versus a 8.1% higher m at $i_{cell} = 0.8\ \mathrm{A/cm^2}$.

The presented method for calculating the performance of fuel cell thermal management systems will be used to analyze key components in more detail in the future. The heat exchanger has a significant impact on the drag, mass, and power demand of the thermal management system. While this study considered a conventional heat exchanger, future enhancements of the method will incorporate new heat exchanger geometries to assess their impact on engine performance. The same applies to the detailed design of the cooling air fan, the air intake, and two-phase cooling concepts. Further potential lies in the coupling of thermal management and hydrogen vaporization. The impact of the thermal management on overall propulsion performance is expected to be even more significant at higher airspeeds. We will therefore extend the method to larger aircraft for up to 50 passengers. The methodology presented thus enables the evaluation of innovative thermal management technologies for fuel cells in aviation.

Nomenclature

Abbreviations

AC	alternating current
DC	direct current
ISA	international standard atmosphere
LT-PEMFC	low-temperature proton-exchange membrane fuel cells

Roman Letters

a	specific work (J/kg)
A	area (m^2)
ALT	altitude (m)
c	velocity (m/s)
c	(drag) coefficient (–)
C	heat capacity rate (W/K)
d	depth (m)
i	current density (A/cm^2)
i	transmission ratio (–)
I	current (A)
f	(Fanning friction) factor (–)
F	Faraday constant (C/mol)
F	thrust (N)
G	mass flow density ($kg/(m^2\,s)$)
h	heat transfer coefficient ($W/(m^2\,K)$)
h	specific enthalpy (J/kg)
LHV	lower heating value (J/kg)
m	mass (kg)
$\dot{m}$	mass flow (kg/s)
M	molar mass (kg/mol)
n	amount of substance (mol)
n	number (–)
NTU	number of transfer units (–)
p	pressure (Pa)
p	specific power ($W\,kg^{-1}$)
P	power (W)
q	specific heat (J/kg)
Q	amount of charge (C)
$\dot{Q}$	heat power (W)
r	radius (m)
Re	Reynolds number (–)
s	specific entropy (J/kg)
t	temperature (°C, K)
SFC	specific fuel consumption (kg s/N)
U	heat transfer coefficient ($W/(m^2\,K)$)
U	voltage (V)
z	charge number (–)

Greek Letters

α	installation angle (°)
δ	wall thickness (m)
ε	effectiveness (–)
η	efficiency (–)
λ	thermal conductivity (W/(m K))
π	total pressure ratio (–)
ρ	density (kg/m^3)
ϕ	cathode humidity (%)

Stations

0	far field air conditions
1	cooling air duct inlet
2	heat exchanger inlet
3	heat exchanger exit
4	cooling air compressor inlet
5	cooling air compressor exit
9	cooling air nozzle exit

12	before propeller
13	behind propeller
19	propeller exit

Sub-/Superscripts

0	standard atmosphere
a	air side
act	active
aux	auxiliary consumers
C	cooling fan
cell	cell
core	heat exchanger core
D	drag
el	electric
EM	electric motor
ext	external
F	propulsive
f	fluid side
FCS	fuel cell system
fr	frontal
GB	gearbox
gr	gross
H_2	hydrogen
HEX	heat exchanger
hyd	hydraulic
in	inlet, input
int	internal
IV	inverter
loss	loss
max	maximum
min	minimum
N	nozzle
o	overall
OCV	open circuit voltage
out	outlet, usable output
P	propeller
p	propulsive
s	isentropic
stack	fuel cell stack
t	total(-pressure, -enthalpy,…)
th	theoretical, thermal
TM	thermal management
w	wall

Appendix A. Reaction equation of the fuel cell and amount of charge

The reaction equation for the anode in a LT-PEMFC is

$$H_2 \rightarrow 2H^+ + 2e^- \tag{A1}$$

and for the cathode

$$\frac{1}{2}O_2 + 2H^+ + 2e^- \rightarrow H_2O, \tag{A2}$$

so that the overall equation is

$$H_2 + \frac{1}{2}O_2 \rightarrow H_2O. \tag{A3}$$

With the Faraday's law

$$Q_{el} = nzF, \tag{A4}$$

the transferred amount of charge is calculated by using the amount of substance n and the charge number z. From the reaction Equation A3 we derive $n_{H_2} = 1$ and that H_2 has to electrons ($z_{H_2} = 2$). Inserting those values into Equation A4 we get

$$Q_{el} = n_{H_2} z_{H_2} F = 2F. \tag{A5}$$

Appendix B. Reactant mass flows

If we insert the definition of the amount of substance

$$n = \frac{m}{M} \tag{B1}$$

into Equation A4 and rearrange it we get

$$m = \frac{Q_{el} M}{zF}. \tag{B2}$$

If we now derive Equation B2 in terms of time, where only Q_{el} is a function of time, we receive

$$\frac{\mathrm{d}m}{\mathrm{d}t} = \frac{\mathrm{d}Q_{el}}{\mathrm{d}t}\frac{M}{zF}. \tag{B3}$$

With the definition of the mass flow

$$\dot{m} = \frac{\mathrm{d}m}{\mathrm{d}t} \tag{B4}$$

and the electric charge

$$Q_{el} = \int I \,\mathrm{d}t \tag{B5}$$

$$\frac{\mathrm{d}Q_{el}}{\mathrm{d}t} = I \tag{B6}$$

we finally arrive at

$$\dot{m} = \frac{I}{zF} M. \tag{B7}$$

Appendix C. Flowchart of the design calculation process

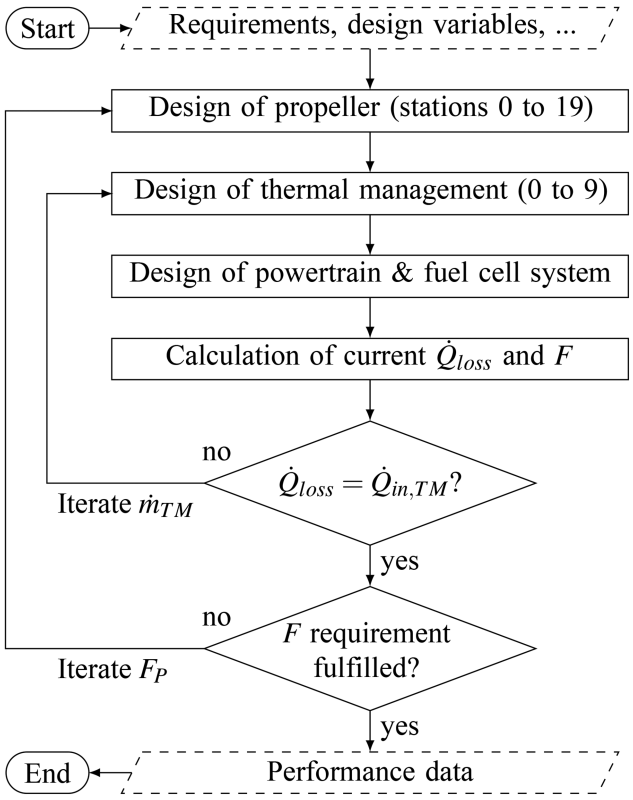

Figure C1. Flowchart of the design calculation process.

Appendix D. Fuel cell system data

Table D1. Design data for the fuel cell system used in the sensitivity study.

Parameter	Value
Auxiliary components factor f_{aux}	0.07
Exhaust gas factor $f_{loss,ext}$	0.05
Stack operating pressure p_{stack}	3 bar
Stack temperature t_{stack}	85 °C
Active cell area $A_{act,cell}$	250 cm^2
Cathode humidity ϕ_{cat}	80%
Specific power of system at $i_{cell} = 1.4\ A/cm^2$ $p_{FCS,1.4}$	2.75 kW/kg

Appendix E. Polarization curve of the designed fuel cell

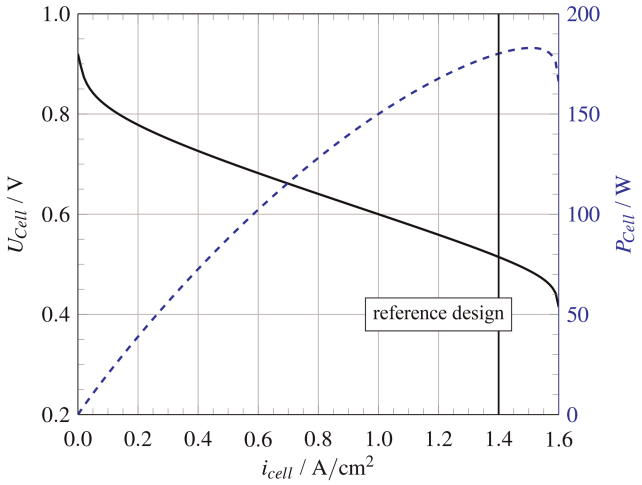

Figure E1. Polarization curve of the fuel cell designed according to Table 4 with U_{cell} and P_{cell} over i_{cell}.

Appendix F. Further component data

Table F1. Design data for the powertrain components used in the sensitivity study.

Parameter	Value
Propeller total pressure ratio π_P	1.003
Isentropic propeller efficiency $\eta_{P,s}$	0.83
Isentropic nozzle efficiency $\eta_{N,s}$	0.999
Isentropic fan efficiency $\eta_{C,s}$	0.85
Inlet total pressure ratio $\pi_{0,2}$	0.98
Nozzle total pressure ratio $\pi_{3,4}$ and $\pi_{5,9}$	0.99
Number of propeller blades n_P	3
Gearbox efficiency η_{GB}	0.98
Gearbox transmission ratio i_{GB}	3.6
Inverter efficiency η_{IV}	0.98
Inverter specific power p_{IV}	12.0 kW/kg
DC/DC converter efficiency η_{DC}	0.99
DC/DC converter specific power p_{DC}	12.0 kW/kg
AC Electric motor efficiency $\eta_{EM,P}$	0.98

(Continued)

Table F1. Continued

Parameter	Value
AC Electric motor spec. power $p_{EM,P}$	9.0 kW/kg
DC Electric motor efficiency $\eta_{EM,C}$	0.98
DC Electric motor spec. power $p_{EM,C}$	7.0 kW/kg

Competing interests

Martin Niehuis declares that he has no conflict of interest. Peter Jeschke declares that he has no conflict of interest.

References

Barbir F. (2013). *PEM fuel cells: theory and practice*. 2nd ed (online-ausg.). Amsterdam and Boston: Elsevier/Academic Press.

Berger O. (2009). Thermodynamische Analyse eines Brennstoffzellensystems zum Antrieb von Kraftfahrzeugen. Dissertation, Universität Duisburg-Essen, Duisburg-Essen.

Bohl W. and Elmendorf W. (2013). *Technische Strömungslehre: Stoffeigenschaften von Flüssigkeiten und Gasen, Hydrostatik, Aerostatik, inkompressible Strömungen, kompressible Strömungen, Strömungsmesstechnik*, 15., überarbeitete und erweiterte auflage edn, Würzburg: Vogel Business Media.

Brown G. V., Kascak A. F., Ebihara B., Johnson D., Choi B., et al. (2005). *NASA Glenn research center program in high power density motors for aeropropulsion: NASA/TM—2005-213800*. Washington, DC, USA.

Chapman J. W., Schnulo S. L., and Nitzsche M. P. (2020). Development of a thermal management system for electrified aircraft. In: 2020 AIAA science and technology forum and exposition (AIAA SciTech Forum). Orlando, Florida, USA: American Institute of Aeronautics and Astronautics.

Drela M. (1996). Aerodynamics of heat exchangers for high-altitude aircraft. *Journal of Aircraft*. 33 (1): 176–184. https://doi.org/10.2514/3.46919.

Eissele J., Lafer S., Mejía Burbano C., Schließus J., Wiedmann T., et al. (2023). Hydrogen-powered aviation—design of a hybrid-electric regional aircraft for entry into service in 2040. *Aerospace*. 10 (3): 277. https://doi.org/10.3390/aerospace10030277.

Hartmann C., Noland J. K., Nilssen R., and Mellerud R. (2022). Dual use of liquid hydrogen in a next-generation pemfc-powered regional aircraft with superconducting propulsion. *IEEE Transactions on Transportation Electrification*. 8 (4): 4760–4778. https://doi.org/10.1109/TTE.2022.3170827.

Hintermayr D. and Kazula S. (2023). Design and analysis of the air inlet system for fuel cell-powered electric propulsion systems in regional aircraft. In: Deutscher Luft- und Raumfahrtkongress 2023. Deutsche Gesellschaft für Luft- und Raumfahrt - Lilienthal-Oberth e.V. Stuttgart, Germany.

Hoerner S. F. (1965). *Fluid-Dynamic Drag: theoretical, experimental and statistical information*.

Jeschke P., Koschel W., Klumpp C., and Weintraub D. (2024). Teaching aero-engine performance: from analytics to hands-on exercises using gas turbine performance software. In: Proceedings of the ASME 2024 Turbomachinery Technical Conference and Exposition. Aachen, Germany: American Society of Mechanical Engineers.

Juschus D. (2021). *Preliminary propulsion system sizing methods for PEM fuel cell aircraft*. Masterthesis, Delft University of Technology, Delft, Niederlande.

Kadyk T., Winnefeld C., Hanke-Rauschenbach R., and Krewer U. (2018). Analysis and design of fuel cell systems for aviation. *Energies*. 11 (2): 375. https://doi.org/10.3390/en11020375.

Kadyk T., Schenkendorf R., Hawner S., Yildiz B., and Römer U. (2019). Design of fuel cell systems for aviation: representative mission profiles and sensitivity analyses. *Frontiers in Energy Research*. 11 (2): 375. https://doi.org/10.3389/fenrg.2019.00035.

Kakaç S., Liu H., and Pramuanjaroenkij A. (2012). *Heat exchangers: selection, rating, and thermal design*. 3rd ed. Boca Raton, Florida, USA: CRC Press, Taylor & Francis Group.

Kays W. M. and London A. L. (2018). *Compact heat exchangers*. 3rd ed. Scientific International, Erscheinungsort nicht ermittelbar. Es tut mir leid, ich kann den Veröffentlichungsort nicht zweifelsfrei ermitteln.

Kazula S., de Graaf S., and Enghardt L. (2023). Review of fuel cell technologies and evaluation of their potential and challenges for electrified propulsion systems in commercial aviation. *Journal of the Global Power and Propulsion Society*. 7: 43–57. https://doi.org/10.33737/jgpps/158036.

Kellermann H., Lüdemann M., Pohl M., and Hornung M. (2021). Design and optimization of ram air–based thermal management systems for hybrid-electric aircraft. *Aerospace*. 8 (1): 3. https://doi.org/10.3390/aerospace8010003.

Kožulović D. (2020). Heat release of fuel cell powered aircraft. In: Proceedings of Global Power and Propulsion Society. Chania, Greece: Global Power & Propulsion Society.

LTH (2022). *Luftfahrttechnisches Handbuch*. Ottobrunn: LTH - Koordinierungsstelle, Ottobrunn.

Manglik R. M. and Bergles A. E. (1995). Heat transfer and pressure drop correlations for the rectangular offset strip fin compact heat exchanger. *Experimental Thermal and Fluid Science*. 10 (2): 171–180. https://doi.org/10.1016/0894-1777(94)00096-Q.

Moffitt B., Bradley T., Mavris D., and Parekh D. (2006). Design space exploration of small-scale PEM fuel cell long endurance aircraft. In: 6th AIAA Aviation Technology, Integration and Operations Conference (ATIO). Reston, Virigina: American Institute of Aeronautics and Astronautics.

Nicolay S., Karpuk S., Liu Y., and Elham A. (2021). Conceptual design and optimization of a general aviation aircraft with fuel cells and hydrogen. *International Journal of Hydrogen Energy*. 46 (64): 32676–32694. https://doi.org/10.1016/j.ijhydene.2021.07.127.

Palladino V., Jordan A., Bartoli N., Schmollgruber P., Pommier-Budinger V., and Benard E. (2021). Preliminary studies of a regional aircraft with hydrogen-based hybrid propulsion. In: AIAA aviation 2021 forum. Reston, Virginia: American Institute of Aeronautics and Astronautics.

Rotax (2021). Coolant radiator for rotax aircraft engines - service instruction: Ata system: 75-00-00 cooling system. https://www.flyrotax.com/p/service/technical-documentation.

Schmelcher M. and Häßy J. (2022). Hydrogen fuel cells for aviation? A potential analysis comparing different thrust categories categories. In: ISABE 2022. Ottawa, Canada: International Society of Air-Breathing Engines.

Shah R. K. and Sekulić D. P. (2003). *Fundamentals of heat exchanger design*. Hoboken NJ: John Wiley & Sons.

Thirkell A., Chen R., and Harrington I. (2017). A fuel cell system sizing tool based on current production aircraft. In: SAE Technical Paper Series. SAE Technical Paper Series, Warrendale, PA, United States: SAE International400 Commonwealth Drive.

ZeroAvia Inc (2023). The hydrogen-electric CESSNA grand caravan white paper: zero-emission, lower cost flight operations in the decade ahead.